NEUROSCIENCE

Wide-field fluorescence lifetime imaging of neuron spiking and subthreshold activity in vivo

Adam J. Bowman[1]*, Cheng Huang[2]†, Mark J. Schnitzer[2,3,4], Mark A. Kasevich[1]*

The development of voltage-sensitive fluorescent probes suggests fluorescence lifetime as a promising readout for electrical activity in biological systems. Existing approaches fail to achieve the speed and sensitivity required for voltage imaging in neuroscience applications. We demonstrated that wide-field electro-optic fluorescence lifetime imaging microscopy (EO-FLIM) allows lifetime imaging at kilohertz frame-acquisition rates, spatially resolving action potential propagation and subthreshold neural activity in live adult *Drosophila*. Lifetime resolutions of <5 picoseconds at 1 kilohertz were achieved for single-cell voltage recordings. Lifetime readout is limited by photon shot noise, and the method provides strong rejection of motion artifacts and technical noise sources. Recordings revealed local transmembrane depolarizations, two types of spikes with distinct fluorescence lifetimes, and phase locking of spikes to an external mechanical stimulus.

Recording the electrical activity of neurons at high spatial and temporal resolution is central to understanding brain function. Fluorescent probes of calcium activity enable optical studies of large neuron populations in vivo (*1*, *2*). However, the response time of calcium indicators is much slower than the underlying electrical signals. Fluorescent voltage sensors are a complementary approach, providing direct readout of neuron membrane potential with the capability to resolve action potentials. Although voltage probes have rapidly developed with a variety of genetically encoded (*3*–*7*) and chemical dyes (*8*) in use, there remain considerable challenges to their application in vivo because of low sensitivity, rapid photobleaching, and motion artifacts. To achieve high-speed recording and sufficient signal-to-noise ratios (SNRs), most voltage probes use fluorescence intensity to read out an underlying sensing mechanism on the basis of absorption, Förster resonance energy transfer (FRET), or quenching.

We applied an alternative strategy for detecting fast probe dynamics that is based on lifetime imaging (*9*). Voltage sensors that use FRET and quenching mechanisms modulate the probe's nonradiative decay rate, intrinsically connecting fluorescence intensity with nanosecond excited-state lifetime. Lifetime is a promising readout for voltage imaging, especially because of its capability to provide an absolute indication of membrane potential (*10*). Recent results have validated fluorescence lifetime for static measurements of membrane potential in vitro (*11*). However, existing lifetime detectors—for example, single-photon counters or cameras with modulated pixels (*12*)—fall short of the requirements for detecting fast dynamics and imaging neurons in vivo, either because of their limited photon throughput or because of prohibitively high noise.

EO-FLIM technique

We demonstrated an approach that uses electro-optic fluorescence lifetime imaging microscopy (EO-FLIM), an all-optical technique for lifetime imaging that is based on nanosecond gating of a wide-field image (*13*, *14*). EO-FLIM allows efficient photon collection and is compatible with detection on high-speed, low-noise scientific cameras. With this method, we achieved lifetime imaging of action potentials in vivo.

EO-FLIM enables significant suppression of intensity artifacts, allowing robust imaging in the presence of tissue motion and fluctuations in illumination intensity. Such artifacts are ubiquitous in recordings of neural activity from awake, behaving animals (*15*, *16*). This has two consequences: (i) It enables faithful recording of subthreshold voltage waveforms, and (ii) it improves the SNR by suppressing high-frequency intensity noise. These follow from the fact that EO-FLIM estimates lifetime from the ratio of a pair of simultaneously recorded intensity channels derived from a common optical source. In conventional approaches, corrections for intensity noise use ratios of measurements that are nonsimultaneous and easily corrupted by high-frequency noise or slower motion artifacts. Optical sensors of neuron activity are typically reported by $\Delta F/F$, referencing fast intensity changes (ΔF) to a nonsimultaneous, average fluorescence baseline (F). Fluorescence lifetime can read out an intensity-optimized sensor with improved temporal noise performance and long-term stability without sacrificing acquisition speed.

We implemented our approach through incorporation of a Pockels cell into the fluorescence detection path of a standard epifluorescence microscope (Fig. 1A, fig. S1, and materials and methods). The Pockels cell design was optimized for resonant drive and wide-field imaging, incorporating thermal control and transverse crystal geometry to cancel off-axis birefringence. A high-voltage modulation was applied to the Pockels cell with a resonant transformer (figs. S2 and S3), resulting in a fast polarization rotation that was synchronous with the excitation pulses from a 100-ps laser source. Fluorescence from the sample was first polarized, then polarization was modulated with the Pockels cell and finally split with a polarizing beamsplitter into two wide-field images on a scientific complementary metal-oxide semiconductor (sCMOS) camera corresponding to gated (G) and ungated (U) intensity. These two images encoded nanosecond time information in their intensity ratio. Because gating was performed with a beamsplitter, it was possible to capture the entire fluorescence decay with photon efficiency limited by optical coatings. In this study, we modulated one input polarization and discarded half of the available signal on a first polarizer. This can be avoided in the future through addition of a second beam path (*13*). The fluorescence decay at each pixel was convolved with the temporal gating function of the Pockels cell and then sampled at a single modulation phase relative to the excitation laser (Fig. 1B). Each image thus provided a lifetime estimate for every pixel in parallel at the frame rate of the scientific camera. When imaging genetically targeted neurons in vivo, this technique allowed for 1-kHz–frame rate recordings with a lifetime sensitivity of 2.53 ± 0.48 ps with 0.7×10^7 to 1.4×10^7 detected photons per frame (Fig. 1C), indicating a substantial improvement in throughput over previous FLIM recordings of cellular dynamics. EO-FLIM approaches fundamental sensitivity limits for estimating lifetimes between 1 and 4 ns (fig. S2).

Results

We used EO-FLIM to image a genetically encoded voltage indicator (GEVI) in *Drosophila melanogaster*. We expressed pAce positive polarity GEVI in a subtype of fly mushroom body output neuron (MBON), MBON-γ1pedc>αβ. pAce works through FRET and is a fusion of the bright fluorescent protein mNeonGreen with a voltage-sensitive opsin from *Acetabularia* (*3*). We surgically prepared *Drosophila* before imaging to provide optical access to the brain (*17*, *18*). Action potentials and subthreshold dynamics were readily resolved with action potentials corresponding to a 20- to 50-ps

[1]Physics Department, Stanford University, Stanford, CA 94305, USA. [2]James H. Clark Center, Stanford University, Stanford, CA 94305, USA. [3]CNC Program, Stanford University, Stanford, CA 94305, USA. [4]Howard Hughes Medical Institute, Stanford University, Stanford, CA 94305, USA.
*Corresponding author. Email: abowman2@stanford.edu (A.J.B.); kasevich@stanford.edu (M.A.K.)
†Present address: Department of Neuroscience, Washington University School of Medicine, St. Louis, MO 63110, USA.

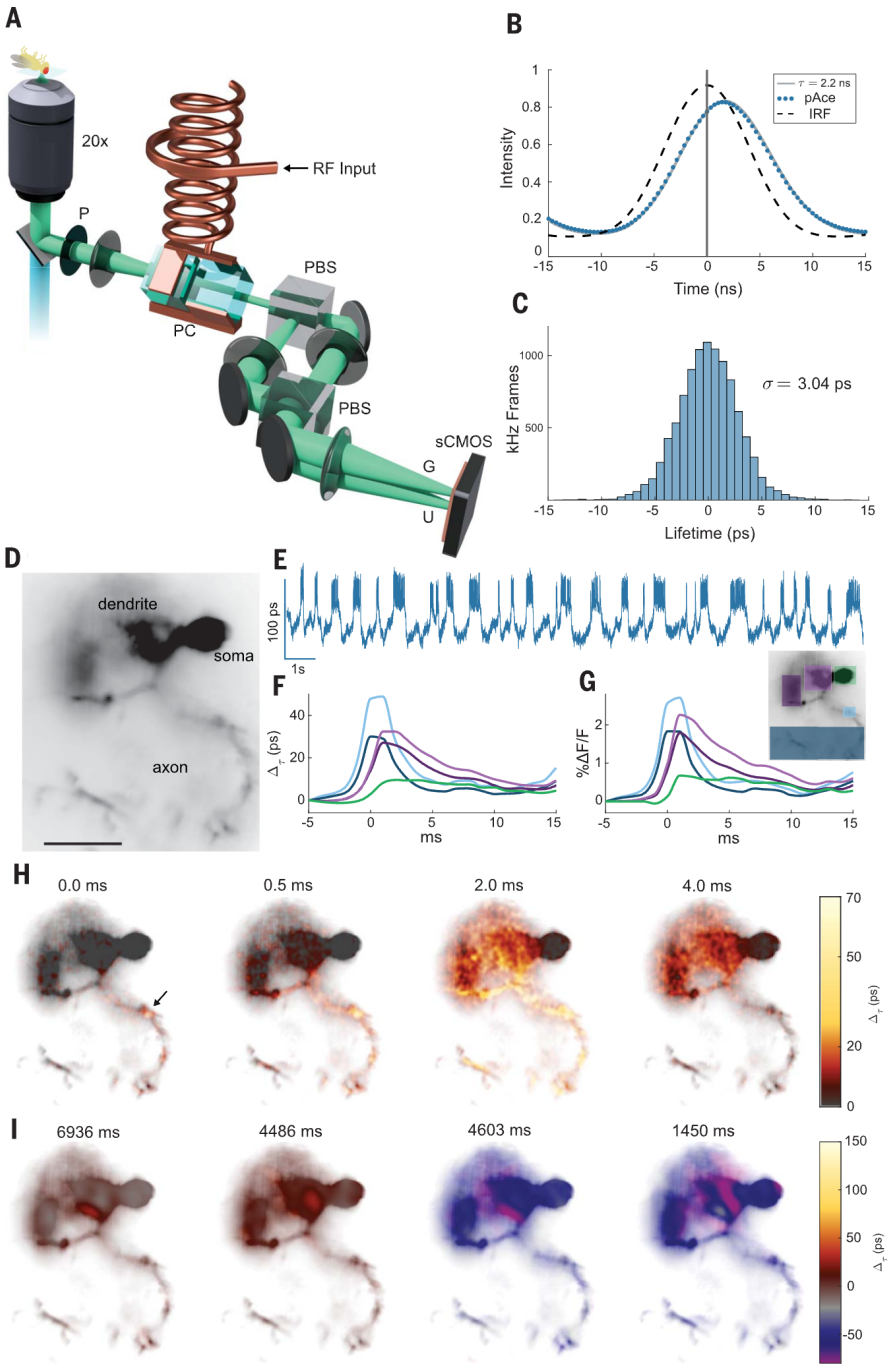

Fig. 1. Lifetime imaging of action potentials. (**A**) Schematic of EO-FLIM microscope. Wide-field fluorescence images were modulated with a Pockels cell (PC) placed between crossed polarizers (P and PBS) and driven at 20 MHz by a high-voltage resonant transformer. Two spatially offset output images were simultaneously captured after a second polarizing beamsplitter (PBS) on a sCMOS camera, corresponding to gated (G) and ungated (U) intensities. (**B**) Instrument response function (IRF) and fluorescence traces for the U channel were measured by varying the Pockels-cell drive phase relative to the excitation laser. The pAce GEVI was fit to 2.2-ns lifetime. For kilohertz imaging, a single optimal phase point was captured (vertical line at 0-ns delay), and the G/U image intensity ratio was converted to a lifetime estimate (fig. S1). (**C**) Histogram of measurements (highpass filtered) obtained at 1 kHz for a single neuron in vivo demonstrate a lifetime sensitivity of 3 ps (full trace in Fig. 2A). (**D**) Wide-field image of a neuron with structures indicated. Scalebar, 25 μm. (**E**) Whole-cell lifetime trace resolves action potentials and subthreshold transitions. (**F** and **G**) Average spike shape is plotted in intensity and lifetime from color-coded regions. (**H**) Frames from an interpolated lifetime movie demonstrate spike propagation, averaging the signal from ~300 individual spikes. The point of initiation is indicated by the arrow, and bidirectional propagation was observed both along the axon and backward toward soma and dendrites (movies S1 to S3). Spike propagation was also imaged directly without averaging (movies S4 and S5). (**I**) Applying a 10-frame moving average allowed subthreshold signals to be localized to neuron structures (movies S6 and S7). Example frames demonstrate localization in the dendrite for both positive and negative subthreshold signals.

shift in the fluorescent lifetime (Fig. 1, D and E). Average spike readouts in lifetime and intensity for different neuron subregions were in strong agreement both in their relative timing and amplitudes (Fig. 1, F and G).

The donor fluorescence lifetime of a FRET GEVI depends on radiative decay rate, k_f, and the voltage-sensitive nonradiative decay rate, $k_{nr}(V)$, associated with FRET as $\tau = \frac{1}{k_f + k_{nr}(V)}$ (*10*, *19*). In pAce, the Ace opsin acts as acceptor and provides voltage sensitivity. The donor's fluorescence intensity is directly quenched by FRET, giving a signal, $\Delta F \propto \sigma \Delta k_{nr}$, where σ is the donor excitation cross section. For an ideal FRET process, one expects to find $\Delta\tau/\tau = \Delta F/F$. pAce gave a linear but attenuated lifetime response of $(0.70 \pm 0.07)\Delta F/F$ (fig. S4). This may indicate components of the GEVI response in intensity—for example, modulation of cross section σ—that did not affect lifetime readout.

Wide-field lifetime imaging correlates neuron activity with spatial structure. The point of action potential initiation in the axon is resolved along with bidirectional propagation along the axon and backward toward the dendrite and soma (*20*). Action potentials were attenuated and broadened in the dendrites and soma (Fig. 1, F and G, and figs. S5 and S6). Spike propagation is shown in movies S1 to S3 with still frames from movie S1 displayed in Fig. 1H, generated with spike-triggered averaging over ~300 spikes and interpolating between frames. We also observed individual spikes and spike propagation in real time without temporal averaging (movies S4 and S5). Comparison of recordings from multiple neuronal subregions revealed local depolarizations in the axons, which fail to initiate action potentials across the entire cell. These depolarizations were not resolved in intensity readout but are clearly visible in lifetime

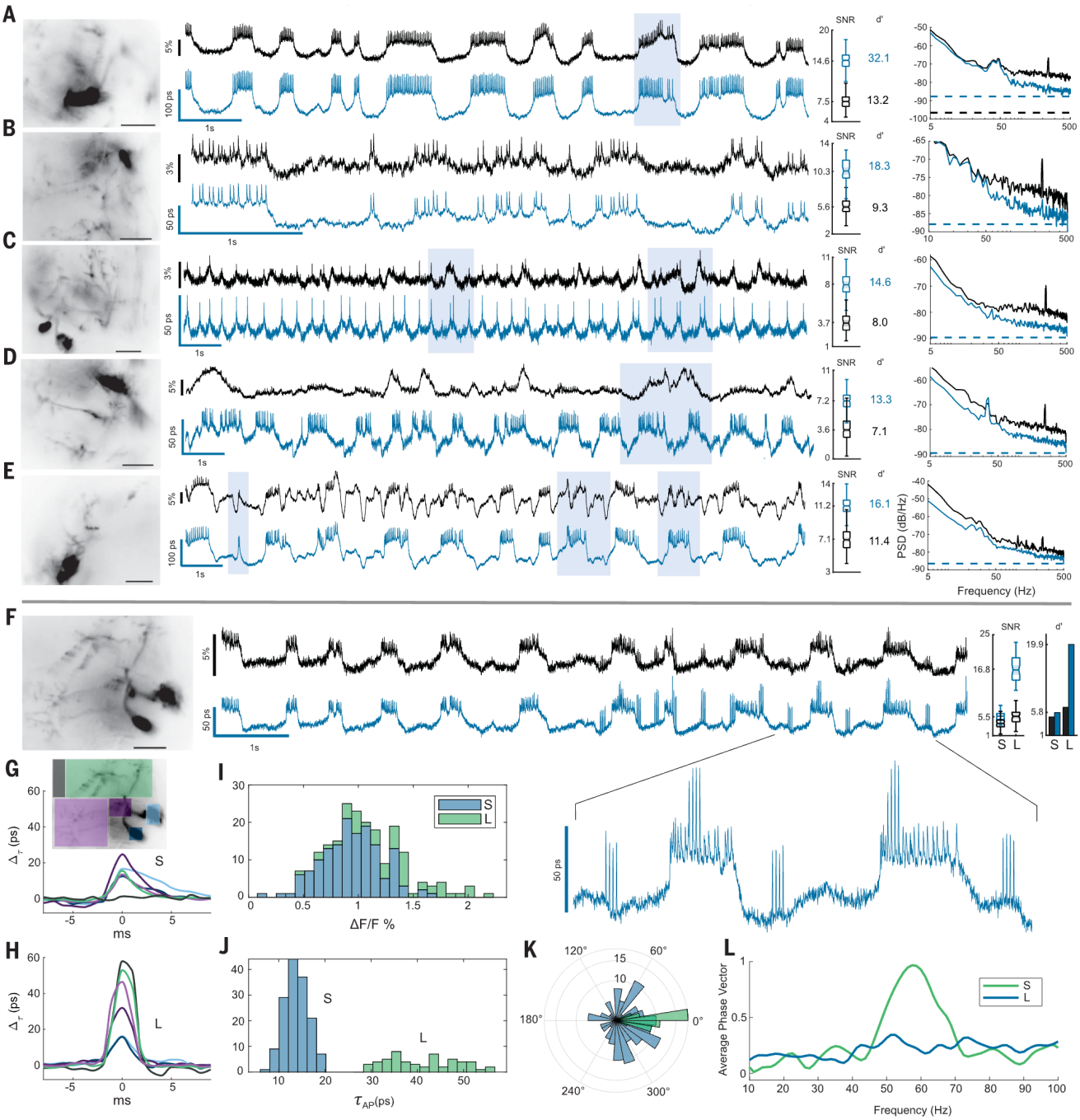

Fig. 2. Lifetime suppresses intensity noise and improves fidelity of subthreshold recording. Six example MBON neurons are shown comparing lifetime (blue) with $\Delta F/F$ intensity recordings (black). Recordings were obtained by averaging over high-resolution images shown at far left. Scalebar, 25 μm. Shaded boxes highlight some notable regions of the traces for improved lifetime readout. For each example, the distributions of spike SNR are compared for intensity and lifetime, with calculated spike detection fidelity d' indicated. (**A** and **B**) Two examples of flies without motion demonstrate improvement of technical noise floor at high frequencies by up to 7 dB. The noise power spectra for the traces are compared at far right, with dotted lines indicating the photon shot-noise limits. (**C** to **E**) Three examples of flies having low-frequency noise associated with motion artifacts. Lifetime improves noise power spectrum across temporal frequencies, rejecting intensity noise by up to 9 dB at low frequencies (further analysis is provided in Fig. 3). (**F** to **J**) Lifetime provided an improved readout of two spike amplitudes in response to mechanical stimulus at 60 Hz. Large-amplitude (L) spikes showed an enhanced lifetime responsivity and tripled detection SNR and d' over the small-amplitude (S) spikes. L spikes occurred independent of subthreshold waveform level but synchronized with spiking on plateaus shown in the inset in (F). (G) and (H) show average spike waveforms for color-coded regions. The point of initiation for S spikes was a central region of the axon (consistent with movies S1 and S2), whereas L spikes were diffuse and associated with background fluorescence. L spikes also correspond to local spikes in the dendrite and soma in (H). The L-spike background component possibly resulted from out-of-focus neurons (movies S8 and S9). In (I) and (J), histograms of action potential amplitudes are compared. In intensity, the L and S populations were not resolved and strongly overlap, but they were clearly separated in lifetime. Lifetime is used to identify the spikes, and the intensity histogram in (I) is shaded with two colors to show overlapping populations. (**K**) A polar histogram demonstrates strong phase locking of the L spikes to mechanical stimulus by referencing phase to a bandpass-filtered lifetime trace. S spikes do not show phase locking. (**L**) The average phase vector length, $\sum_i \cos(\theta_i)/N_{AP}$, is plotted versus bandpass center frequency to show narrow-band locking response.

recordings (figs. S5 and S6). When we then applied a 10-frame moving average, the spatial distribution of slower subthreshold voltage signals could also be studied. Subthreshold signals were often strongest and localized in the dendrites (movies S6 and S7). Still frames from these movies are shown in Fig. 1I and figs. S7 and S8.

By measuring a ratio of simultaneous intensities, EO-FLIM removes noise sources that are common mode to both the modulated channels. In Fig. 2, we show example recordings of MBON-γ1pedc>α/β neurons from six flies, comparing intensity $\Delta F/F$ with lifetime readouts. In all recordings, lifetime detection enhanced the SNR for action potential detection by approximately twofold. This SNR was quantified by comparing spike amplitude with the high-frequency noise floor. We also analyzed traces by using the spike detection fidelity, *d′*, a discriminability index that quantifies spike detection by comparing the statistical distributions of spike amplitudes and background-noise fluctuations (*21*). Lifetime detection improved *d′* by 1.5 to 2.4 times (Fig. 2, A to E).

Noise power was also compared across temporal frequencies, demonstrating broad suppression of intensity noise (Fig. 2, A to E) and showing that EO-FLIM approaches the photon shot-noise limit. To allow a direct comparison of noise power spectrum, the responsivity of spikes in intensity and lifetime channels was normalized. For flies not displaying much motion (Fig. 2, A and B), lifetime primarily reduced technical noise at high frequencies that resulted from the excitation laser (4 to 7 dB). Even in these well-behaved examples, lifetime readout resulted in improved SNR and *d′*.

Lifetime recordings also improved long-term stability in the voltage readout. Intensity-based voltage imaging often displays strong motion artifacts, which degrade stability. In *Drosophila*, these artifacts result from movements such as extension of the proboscis. For flies displaying motion (Fig. 2, C to E, and fig. S9), lifetime readout suppressed artifacts at low frequencies by up to 9 dB as compared with intensity readout (in these examples, subthreshold waveforms may only be resolved in lifetime). Figure 3 shows trace stability quantified according to the spike-amplitude distribution and the uniformity of threshold voltage level at action potential locations. Histograms of mean normalized spike heights and mean normalized subthreshold level are plotted for each spike, showing that lifetime improves spike uniformity by up to 2.5 times and threshold uniformity by up to 5.8 times.

With the improved readout stability afforded by lifetime recording, we observed two spike amplitudes (Fig. 2, F to L). The small-amplitude (S) spikes occurred on top of subthreshold voltage plateaus, whereas large-amplitude (L) spikes were observed in bursts that were independent of subthreshold voltage level. In this sample, the fly was mechanically stimulated with sound waves near a resonance of the microscope stage. Figure 2, I and J, show histograms of spike heights in both intensity and lifetime. The two spike populations were clearly distinguished by using lifetime readout but were not separable with intensity readout. The L spikes showed enhanced lifetime responsivity (1.34 $\Delta F/F$, compared with 0.68 $\Delta F/F$ for S spikes). The difference in responsivity may indicate kinetic differences in the GEVI response to different action potential waveforms (*3*). Spike-triggered averages (movies S8 and S9) showed that the L spikes originated diffusely across the image, whereas the S spikes initiated in a local area of the axon, as shown in movies S1 and S2. The L spikes may be associated with out-of-focus neurons displaying off-target GEVI expression and were also synchronous with spiking of the targeted neuron (Fig. 2, F to H). The L spikes displayed strong phase locking in response to mechanical stimulus, whereas the S spikes did not. A histogram of phases is displayed in Fig. 2K, where phase is determined by each spike's location on a trace that has been filtered at the stimulus frequency. Narrow-band locking response is demonstrated in Fig. 2L. Similar L spikes were also observed during the mechanical stimulus sweep (Fig. 4C).

To further demonstrate the noise-rejection capabilities of lifetime detection, we placed the fly on a piezoelectric stage to provide mechanical shaking in the *xy* plane. This

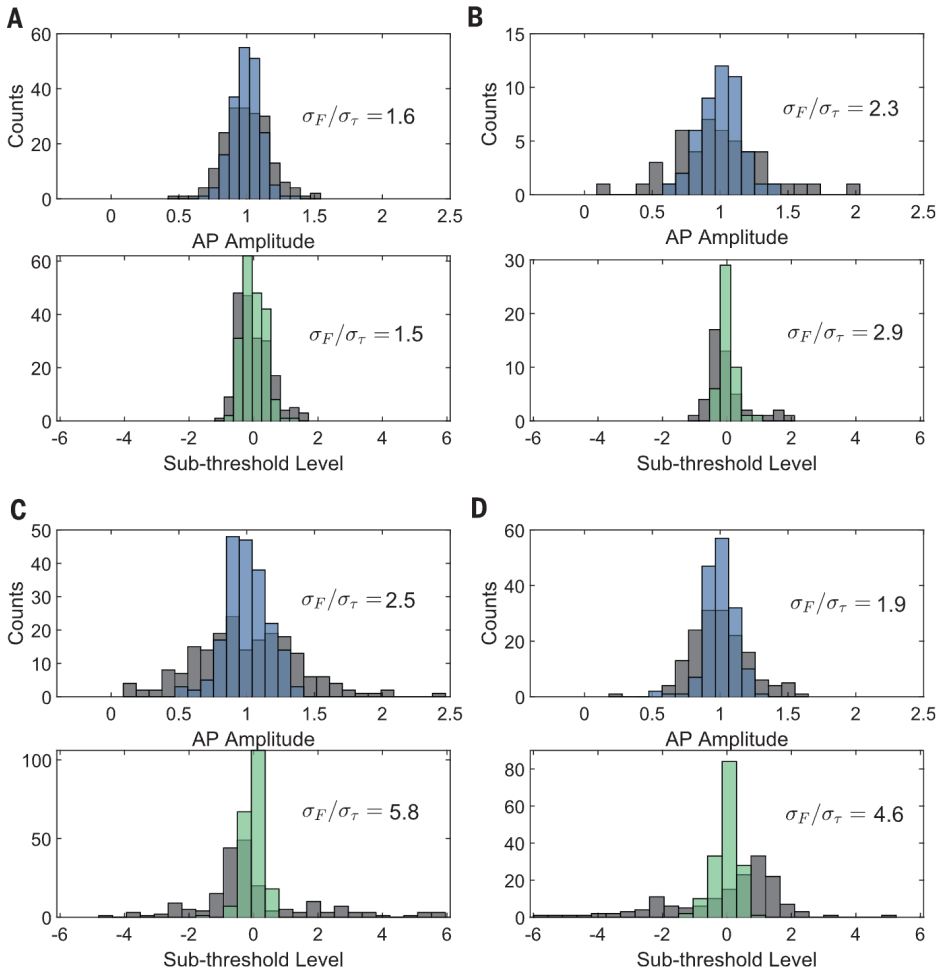

Fig. 3. Lifetime improves uniformity in action potential amplitude and threshold level. (**A** to **D**). Histograms of action potential amplitudes (lifetime in blue) and action potential levels on the subthreshold waveform (lifetime in green) are plotted for each activity trace, overlayed on the same histograms for intensity (gray). Action potential amplitudes are normalized to the mean. Subthreshold level is also mean normalized as $(L-\bar{L})/\bar{L}$, where L is the spike's corresponding level on a low-pass filtered trace, and its distance is measured relative to the mean level of all other spikes, $\bar{L}$. A perfectly uniform threshold would thus result in $L = 0$ for all spikes. In each histogram, the ratio of standard deviation between intensity and lifetime readouts, σ_F/σ_τ, is given as a figure of merit for uniformity. (A) and (B) to (D) correspond to Fig. 2, A and C to E, respectively.

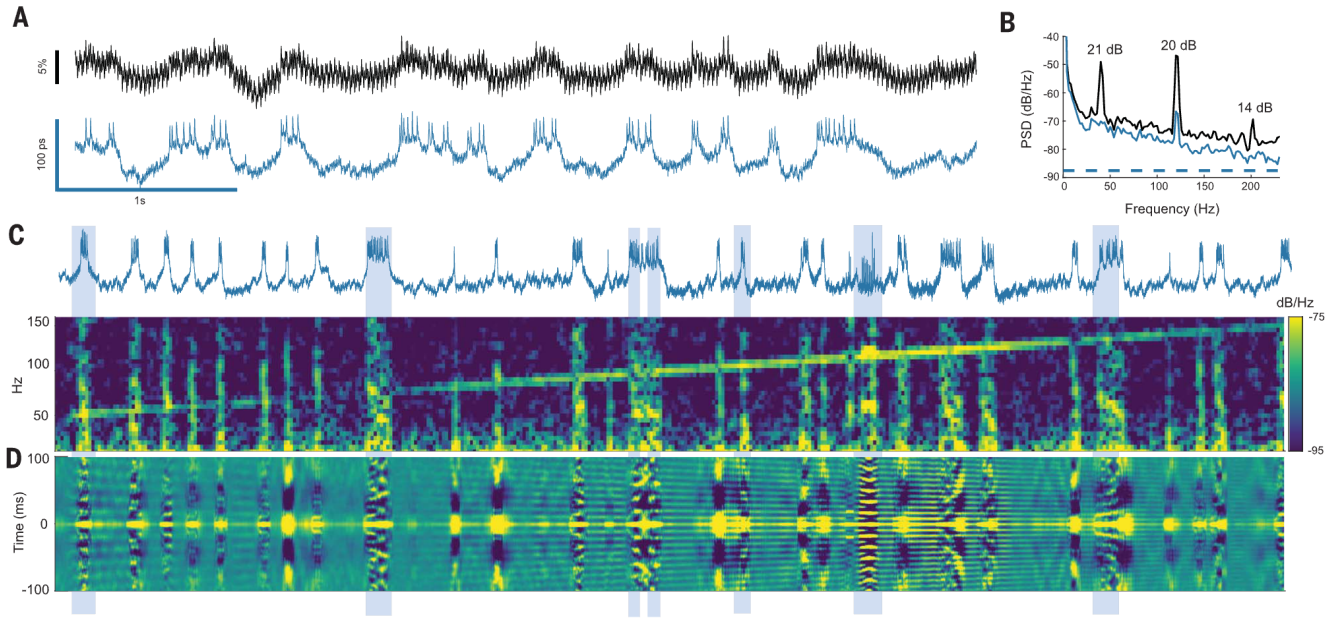

Fig. 4. Phase locking of spikes to direct mechanical stimulus. (**A**) Lifetime provided strong rejection of intensity noise associated with shaking the sample (40-Hz square wave, ~0.8 μm peak-to-peak). (**B**) Intensity noise at the stimulus frequency and second harmonic were attenuated by 21 and 20 dB. (**C**) A spectrogram of the lifetime trace is plotted as stimulus is swept from 50 to 150 Hz. Vertical lines of activity in the spectrogram correspond to spike bursts in the lifetime trace. Mechanical cross-talk is seen as the diagonal line sweep, and phase locking appears as increased frequency content at the stimulus frequency during spike bursts. (**D**) To show phase locking visually, a sliding window autocorrelation of the lifetime trace is plotted with a 150-ms window. Phase locking may be seen by observing alignment of autocorrelation peaks during activity bursts to the peaks resulting from mechanical cross-talk signal. Examples of bursts showing phase locking are highlighted (blue vertical bars).

direct mechanical stimulus resulted in high levels of intensity noise that obscured neuron activity, but lifetime readout suppressed this noise by up to 21 dB (Fig. 4, A and B). Using this direct stimulus, we could observe phase-locked spiking behavior from 30 to >100 Hz (Fig. 4 and fig. S10). As shown in these figures, we observed phase locking through increased spectral power at the stimulus frequency in a spectral waterfall plot as the excitation frequency was swept. This phase locking may also be visualized with the autocorrelation of the lifetime trace (Fig. 4, C and D). These observations are consistent with previous studies on mechanical and auditory effects in *Drosophila* that identified a broad auditory response across the central brain (*22*) and responses to substrate vibrations (*23*, *24*).

Discussion

EO-FLIM may be applied to both existing lifetime-sensitive probes and to donor readout of FRET-based biosensors. Standard FRET sensors are read out by the ratio of optical intensities in spectrally separated donor and acceptor channels (*25*), requiring an acceptor molecule with high quantum yield. Two-color readout frequently limits detection sensitivity because of spectral cross-talk and also prevents probe multiplexing (*26*). Lifetime measurement removes these limitations and allows quantitative FRET measurements with only the donor channel. In voltage imaging, lifetime will enable improved measurement of FRET-opsin (*3*, *7*), hybrid FRET (*6*), and dye indicators (*8*). We also anticipate application to imaging calcium (*27*), neurotransmitters (*28*, *29*), and cyclic adenosine monophosphate (*30*).

Use of GEVIs in vivo is often accompanied by a large fluorescence background that results from protein expression outside the cellular membrane (*31*) or leaky gene expression from nontargeted cells (*32*). This background signal had a different fluorescence lifetime and photobleaches at a different rate, resulting in slow drifts of the measured lifetime traces (fig. S11). (We expect that in vitro studies will not be affected by such backgrounds.) To measure absolute voltage, signal and background populations would need to be unmixed by discriminating between two closely spaced exponential decays. For this reason, we focus on the improved stability and noise performance afforded by lifetime measurement rather than on absolute quantification. In our current implementation, we measured the population-weighted average lifetime by acquiring images at a single modulation phase. In the future, multiple modulation phases can be combined to unmix lifetime components and improve absolute measurement.

We have shown that EO-FLIM enables fluorescence lifetime imaging of neuron activity in vivo, overcoming the throughput and sensitivity limitations of existing FLIM techniques. We expect straightforward application to other systems, including mammalian brains, which feature both larger neurons and action potentials as compared with those of *Drosophila* (*3*, *7*). Voltage imaging in neuroscience is one example application, but membrane potential is also broadly interesting throughout biology, from bacteria (*33*, *34*) and plants (*35*) to cardiac (*36*–*38*) and muscle tissue (*39*). The ability of EO-FLIM to strongly reject motion noise in vivo is relevant for brain- and cardiac-imaging applications in which it is challenging to faithfully distinguish voltage dynamics from motion and hemodynamic artifacts (*15*, *16*, *36*, *37*). It may become possible to perform voltage imaging during natural movements such as insect flight, or while tracking a freely moving organism (*40*). Further, recent advances in GEVI probes have enabled voltage imaging of populations of neurons (*3*, *5*). Lifetime imaging will establish accurate long-term readout of subthreshold activity across a neural circuit, allowing functional connectivity mapping where spike activity may be correlated with subthreshold modulation of downstream neurons. Last, by using lifetime detection in combination with optogenetic tools (*4*, *41*), it will be possible to improve techniques for targeted optical activation and control (*42*) of neuron membrane potential.

REFERENCES AND NOTES

1. T. H. Kim, M. J. Schnitzer, *Cell* **185**, 9–41 (2022).
2. M. B. Ahrens, M. B. Orger, D. N. Robson, J. M. Li, P. J. Keller, *Nat. Methods* **10**, 413–420 (2013).
3. M. Kannan *et al*., *Science* **378**, eabm8797 (2022).
4. H. Tian *et al*., All-optical electrophysiology with improved genetically encoded voltage indicators reveals interneuron network dynamics in vivo, bioRxiv 2021.11.22.469481 [Preprint] (2021). https://doi.org/10.1101/2021.11.22.469481.
5. K. D. Piatkevich *et al*., *Nature* **574**, 413–417 (2019).
6. A. S. Abdelfattah *et al*., *Science* **365**, 699–704 (2019).
7. Y. Gong *et al*., *Science* **350**, 1361–1366 (2015).
8. P. Liu, E. W. Miller, *Acc. Chem. Res.* **53**, 11–19 (2020).
9. R. Datta, T. M. Heaster, J. T. Sharick, A. A. Gillette, M. C. Skala, *J. Biomed. Opt.* **25**, 071203 (2020).
10. D. Brinks, A. J. Klein, A. E. Cohen, *Biophys. J.* **109**, 914–921 (2015).
11. J. R. Lazzari-Dean, A. M. Gest, E. W. Miller, *eLife* **8**, e44522 (2019).
12. M. Raspe *et al*., *Nat. Methods* **13**, 501–504 (2016).
13. A. J. Bowman, M. A. Kasevich, *ACS Nano* **15**, 16043–16054 (2021).
14. A. J. Bowman, B. B. Klopfer, T. Juffmann, M. A. Kasevich, *Nat. Commun.* **10**, 4561 (2019).
15. J. D. Marshall *et al*., *Cell* **167**, 1650–1662.e15 (2016).
16. M. S. Creamer, K. S. Chen, A. M. Leifer, J. W. Pillow, *PLOS Comput. Biol.* **18**, e1010421 (2022).
17. S. Sinha *et al*., *Proc. Natl. Acad. Sci. U.S.A.* **110**, 18374–18379 (2013).
18. C. Huang *et al*., *Nat. Commun.* **9**, 872 (2018).
19. R. M. Clegg, in *FRET and FLIM Techniques*, T. W. J. Gadella, Ed., vol. 33 of *Laboratory Techniques in Biochemistry and Molecular Biology* (2009), pp. 1–57.
20. C. Huang *et al*., Dopamine signals integrate innate and learnt valences to regulate memory dynamics, Research Square [Preprint], Version 1 (2022). https://assets.researchsquare.com/files/rs-1915648/v1_covered.pdf?c=1660253275.
21. B. A. Wilt, J. E. Fitzgerald, M. J. Schnitzer, *Biophys. J.* **104**, 51–62 (2013).
22. D. A. Pacheco, S. Y. Thiberge, E. Pnevmatikakis, M. Murthy, *Nat. Neurosci.* **24**, 93–104 (2021).
23. P. Hehlert, W. Zhang, M. C. Göpfert, *Trends Neurosci.* **44**, 323–335 (2021).
24. W. Zhang, Z. Yan, L. Y. Jan, Y. N. Jan, *Proc. Natl. Acad. Sci. U.S.A.* **110**, 13612–13617 (2013).
25. W. Akemann *et al*., *J. Neurophysiol.* **108**, 2323–2337 (2012).
26. D. M. Grant *et al*., *Biophys. J.* **95**, L69–L71 (2008).
27. F. H. van der Linden *et al*., *Nat. Commun.* **12**, 7159 (2021).
28. P. Ma *et al*., Fluorescence lifetime enables high-resolution analysis of neuromodulator dynamics across time and animals, bioRxiv 2022.09.28.510014 [Preprint] (2022). https://doi.org/10.1101/2022.09.28.510014.
29. L. Sistemich, P. Galonska, J. Stegemann, S. Kruss, *Angew. Chem. Int. Ed. Engl.* **62**, e202300682 (2023).
30. J. Klarenbeek, J. Goedhart, A. van Batenburg, D. Groenewald, K. Jalink, *PLOS ONE* **10**, e0122513 (2015).
31. J. Platisa, V. A. Pieribone, *Curr. Opin. Neurobiol.* **50**, 146–153 (2018).
32. Y. Aso *et al*., *eLife* **3**, e04577 (2014).
33. A. Prindle *et al*., *Nature* **527**, 59–63 (2015).
34. J. M. Kralj, D. R. Hochbaum, A. D. Douglass, A. E. Cohen, *Science* **333**, 345–348 (2011).
35. N. B. C. Serre *et al*., *Nat. Plants* **7**, 1229–1238 (2021).
36. C. D. Acker, P. Yan, L. M. Loew, *Prog. Biophys. Mol. Biol.* **154**, 3–10 (2020).
37. P. Lee *et al*., *Cardiovasc. Res.* **115**, 1659–1671 (2019).
38. J. P. Wikswo Jr., S. F. Lin, R. A. Abbas, *Biophys. J.* **69**, 2195–2210 (1995).
39. N. Azimi Hashemi *et al*., *Proc. Natl. Acad. Sci. U.S.A.* **116**, 17051–17060 (2019).
40. J. P. Nguyen *et al*., *Proc. Natl. Acad. Sci. U.S.A.* **113**, E1074–E1081 (2016).
41. Y. Adam *et al*., *Nature* **569**, 413–417 (2019).
42. A. C. F. Bergs *et al*., *Nat. Comm.* **14**, 1939 (2023).
43. A. J. Bowman, C. Huang, M. J. Schnitzer, M. A. Kasevich, Wide-field fluorescence lifetime imaging of neuron spiking and sub-threshold activity in vivo, Dryad (2023); https://doi.org/10.5061/dryad.nzs7h44wd.
44. A. J. Bowman, C. Huang, M. J. Schnitzer, M. A. Kasevich, Wide-field fluorescence lifetime imaging of neuron spiking and sub-threshold activity in vivo, Version 1, Zenodo, (2023); https://doi.org/10.5281/zenodo.7706488.

ACKNOWLEDGMENTS

Funding: We acknowledge funding from the Gordon and Betty Moore Foundation; the US Department of Energy, Office of Science, Office of Biological and Environmental Research, under award DE-SC0021976; NIH grant U01NS120822 (M.J.S. and G. Vasan); and NSF NeuroNex grant DBI-1707261 (M.J.S. and K. Deisseroth). A.J.B. acknowledges support from the NSF Graduate Research Fellowship under grant 1656518 and the Stanford Graduate Fellowship. **Author contributions:** A.J.B. developed the microscope. C.H. prepared *Drosophila* for imaging. A.J.B. and C.H. performed the experiments. A.J.B. and M.A.K. analyzed data and wrote the manuscript. All authors contributed to experiment conception and manuscript revision. **Competing interests:** A.J.B. and M.A.K. are inventors on PCT/US2019/062640, US17/153438, and US17/898093. **Data and materials availability:** All data are available in the manuscript, in the supplementary material, or deposited at Dryad (*43*). Code is available at Zenodo (*44*).

SUPPLEMENTARY MATERIALS

science.org/doi/10.1126/science.adf9725
Materials and Methods
Figs. S1 to S11
Movies S1 to S9
MDAR Reproducibility Checklist

View/request a protocol for this paper from *Bio-protocol*.

Submitted 23 November 2022; accepted 16 May 2023
10.1126/science.adf9725